# Relationship between the microstructure and nanoindentation hardness of thermally evaporated and magnetron-sputtered electrochromic tungsten oxide films

C.W. Ong,[a)] H.Y. Wong, G.K.H. Pang, K.Z. Baba-Kishi, and C.L. Choy
*Department of Applied Physics and Materials Research Center, The Hong Kong Polytechnic*
*University, Hung Hom, Kowloon, Hong Kong, People's Republic of China*

Tungsten oxide ($WO_x$) films were fabricated by (i) reactive thermal evaporation (RTE) at room temperature with oxygen ambient pressure $P_{O_2}$ as a parameter, and (ii) reactive magnetron sputtering (RMS) with substrate temperature $T_s$ as a parameter. The film structure revealed by x-ray photoelectron spectroscopy, x-ray diffraction, density measurements, infrared absorption, and atomic force microscopy was correlated with the nanoindentation hardness $H$. The RTE $WO_x$ films deposited at high $P_{O_2}$ were amorphous and porous, while $H$ depended appreciably on normalized penetration depth $h_D$ (indentation depth/film thickness) due to the closing of the pores at the point of indentation. Decrease in $P_{O_2}$ from 10 to $2 \times 10^{-3}$ mtorr led to smaller porosity, weaker $h_D$ dependence of $H$, and higher average $H$ (measured at $h_D \approx 0.2$ to 0.3, for example). The RMS $WO_x$ film deposited at room temperature was amorphous and denser than all RTE films. The rise in substrate temperature $T_s$ first densified the film structure (up to 110 °C) and then induced crystallization with larger grain size for $T_s \geqslant 300$ °C. Correspondingly, the $h_D$ dependence of $H$ became weaker. In particular, $H$ of the RMS sample deposited at 110 °C showed a peak at $h_D$ slightly above 1 owing to pileup at the contact point of indentation. For higher $T_s$, pileup occurred at shallower $h_D$ and the average $H$ (measured at $h_D \approx 0.2$ to 0.3, for example) rose, accompanied by the increase of grain size.

## I. INTRODUCTION

Tungsten oxide ($WO_x$) is of great potential in the application of electrochromic devices (ECD) because of its high coloration efficiency.[1–9] In the past few decades, great effort has been made to investigate the relation between the fabrication techniques and conditions, microstructure, electrochromic properties, and degradation mechanisms in $WO_x$ films during color–bleach (c/b) switching cycles. It is found that the fabrication techniques and conditions indeed have a strong influence on the microstructure, which in turn governs the electrochromic behavior and degradation of the films.[10] On the other hand, the mechanical properties of $WO_x$ films have received relatively little attention, but they deserve more investigation because they are also closely related to the microstructure and can affect the durability and stability of the devices associated with any mechanical damages.

The objective of this work was to study the relation between the microstructure and the mechanical properties of $WO_x$ films fabricated by techniques, namely, reactive

thermal evaporation (RTE) and reactive magnetron sputtering (RMS), under different conditions. For the RTE processes, oxygen ambient pressure was varied as a parameter, while the substrate temperature was kept at 25 °C. For the RMS processes, substrate temperature was the main preparation parameter. Cyclic voltametry (CV) was employed to illustrate the electrochromic properties of some selected samples. The film composition and structure were investigated by x-ray photoelectron spectroscopy (XPS), density measurements, x-ray diffraction (XRD), infrared absorption (IR), and atomic force microscope (AFM). The mechanical properties, in terms of the penetration depth dependence of hardness and elastic modulus, were recorded by nanoindentation techniques. The hardness and elastic modulus data of films fabricated by different preparation methods and conditions were interpreted according to the results of structural analyses.

## II. SAMPLE PREPARATION

By thermally evaporating tungsten trioxide powder (99.99% $WO_3$) placed in a tungsten boat, $WO_x$ films (hereafter called RTE films) were deposited on indium

---
[a)]Address all correspondence to this author.
 e-mail: apacwong@hkpucc.polyu.edu

tin oxide (ITO, 30 nm thick, electrical conductivity $= 3.3 \times 10^3 \ \Omega^{-1} \ cm^{-1}$) coated glass plates placed 20 cm above the boat. The substrate was kept at room temperature and the oxygen ambient pressure $P_{O_2}$ was varied from 10 to $2 \times 10^{-3}$ mtorr by a mass flow controller. As shown in Table I, the thicknesses of the films varied from 177 to 214 nm.

RMS WO$_x$ films were deposited by sputtering a tungsten target (99.95%) with a 2-in. magnetron sputtering gun, direct current (dc) powered at 80 W. The ITO-coated glass substrate was placed 16 cm from the target. For the preparation of RMS1 to RMS4 (Table I), the substrate temperature $T_s$ was varied from 25 to 500 °C, while the gas flow ratio of oxygen to argon ($[O_2]/[Ar]$) was kept constant at 2. RMS5 and RMS6 were deposited with no substrate heating, and smaller $[O_2]/[Ar]$ ratios of 1.75 and 1.36 were used. For all RMS films, the total ambient pressure was fixed at 10 mtorr. The film thickness $t$ varied from 117 to 638 nm.

## III. CHARACTERIZATION

The cyclic voltammograms of samples RTE2 and RMS1 were recorded using an EG&G Model 273 voltameter, with the change in their optical transmittance being monitored concurrently. The sample was immersed in a 1 M LiClO$_4$-propylene carbonate solution. The working, counter, and reference electrodes in the circuit were the ITO coating, a platinum wire, and a saturated calomel electrode (SCE), respectively. An alternating voltage (amplitude = 1.2 or 2 V) was applied between the working and reference electrodes. The current passing through the working electrode was recorded. The corresponding change in the optical transmittance of the film was monitored simultaneously using a photodiode, which detected the intensity of a HeNe laser beam passing through the sample.

A Phi Quantum 2000 XPS system equipped with a monochromatic Al K$_\alpha$ radiation source was used to collect the W4$f$, O1$s$, and C1$s$ photoelectron spectra. The ratio of the relative contents of the elements is equal to

that of the integrated areas above the Shirley background[11] normalized with respect to the corresponding sensitivity factors, namely 0.733, 3.863, and 0.314 for the W4$f$, O1$s$, and C1$s$ photoelectrons, respectively. A Philips X'PERT x-ray diffractometer (Cu K$_\alpha$ radiation) with thin film optics was used to examine the crystallinity of the samples. The theta drive was locked at a grazing angle of 0.65°, and the 2θ angle was scanned from 15 to 75°. The IR absorption spectra of the films in the wave number range of 400–4000 cm$^{-1}$ were recorded using a Nicolet's Magna-TR™ System model 750 Fourier transform infrared absorption spectrometer. The density of the films was calculated from the thickness determined by an α-step surface profiler (Tencor P-10, accuracy ±1 nm), and the mass was obtained from the change in the weight of the substrate before and after deposition using an electronic balance (Mettler AT201, accuracy ±0.005 mg). The error of the calculated density was estimated according to the principle of error propagation. A Burleigh Metris-2000NC atomic force microscope (AFM) working in tapping mode (resonant peak = 185.5 kHz) was used to investigate the surface morphology. Both the topographic and phase contrast images were recorded. The phase contrast imaging method detects the phase difference between the cantilever's oscillation and the input signal for driving the piezoelectric crystal[12] and can reveal the fine details of a rough surface.

A Nanoindenter IIs (Nano Instruments, Inc.) was used to measure the hardness $H$ and elastic modulus $E$ of the films without experiencing color–bleach cycles. The load frame stiffness and area function of the diamond tip were calibrated carefully prior to the measurements.[13] Six indentation experiments were made to cover a load range of 10 μN to 300 mN. An experiment consisted of three loading segments with progressively increasing maximum loads. Each experiment was repeated five times at different locations. Data collected at the same specified load were averaged to get $H$ and $E$ at a depth. The values of $H$ and $E$ were extracted from the load-displacement data according to method described by Oliver *et al.* It is assumed that intrusion of tip induces both plastic and

TABLE I. Summary of the results of RTE and RMS WO$_x$ films. $H$ and $E$ are the average values of data recorded at indentation depths around $h_D = 0.2$ to $0.3$.

| Sample | $[O_2]/[Ar]$ | $P_{O_2}$ (mtorr) | $T_s$ (°C) | $t$ (nm) | O/W | Density (g cm$^{-3}$) | $H$ (GPa) | $E$ (GPa) |
|--------|-----------|-----------|-------|------|------|-----------------|-------------|-----------|
| RTE1 | — | 10 | 25 | 177 | 3.5 | 4.1 ± 0.32 | 0.96 ± 0.1 | 43.5 ± 3 |
| RTE2 | — | 6 | 25 | 184 | 3.4 | 4.5 ± 0.43 | 1.3 ± 0.1 | 43.6 ± 3 |
| RTE3 | — | 4 | 25 | 214 | 3.6 | 4.7 ± 0.33 | 2.1 ± 0.1 | 54.7 ± 2 |
| RTE4 | — | $2 \times 10^{-3}$ | 25 | 210 | 3.6 | 6.9 ± 0.52 | 3.2 ± 0.2 | 80.1 ± 1 |
| RMS1 | 2 | — | 25 | 420 | 2.9 | 7.7 ± 0.32 | 3.0 ± 0.2 | 79.6 ± 4 |
| RMS2 | 2 | — | 110 | 117 | 2.9 | 7.3 ± 0.77 | 5.6 ± 0.2 | 95.8 ± 4 |
| RMS3 | 2 | — | 300 | 152 | 3.0 | 7.5 ± 0.72 | 5.7 ± 0.5 | 92.0 ± 6 |
| RMS4 | 2 | — | 500 | 406 | 3.0 | 7.7 ± 0.60 | 7.8 ± 0.3 | 94.4 ± 2 |
| RMS5 | 1.75 | — | 25 | 485 | 2.70 | 8.7 ± 0.24 | 4.6 ± 0.2 | 82.2 ± 2 |
| RMS6 | 1.36 | — | 25 | 638 | 2.41 | 10.5 ± 0.16 | 6.4 ± 0.3 | 107 ± 3 |

1542    CAMBRIDGE JOURNALS

J. Mater. Res., Vol. 16, No. 6, Jun 2001

elastic deformations, and during unloading the elastic deformation recovers first. The unloading curve is fitted to the formula:

$$P = B(h - h_f)^m \quad , \tag{1}$$

where *B, m,* and the final displacement after complete unloading $h_f$ are fitting parameters. The slope of the unloading curve at the maximum load $P_{max}$ (corresponding to the maximum displacement $h_{max}$) is thereby assumed to be the unloading stiffness:

$$S = \left.\frac{dP}{dh}\right|_{h=h_{max}} = mB\,(h_{max} - h_f)^{m-1} \quad . \tag{2}$$

The contact depth $h_c$ between the tip and the surface associated with the plastic deformation is determined to be

$$h_c = h_{max} - \epsilon\,P_{max}/S \quad , \tag{3}$$

where $\epsilon$ is a constant set at 0.75 for a tip with parabolic rotation symmetry. The contact area *A* at the contact depth is then obtained from the calibrated tip area function. The hardness *H* and elastic modulus *E* of the sample are then given by

$$H = P_{max}/A(h_c) \quad , \tag{4}$$

and

$$\frac{1-\nu^2}{E} + \frac{1-\nu_i^2}{E_i} = \frac{\sqrt{\pi}}{2}\frac{S}{\sqrt{A(h_c)}} \quad , \tag{5}$$

where $\nu$ is the Poisson's ratio of the sample assumed to be 0.25, and $\nu_i$ and $E_i$ are the Poisson's ratio and elastic modulus of diamond, which are equal to 0.07 and 1141 GPa, respectively.

## IV. RESULTS AND DISCUSSION

### A. Electrochromic properties

In Fig. 1, the cyclic voltammograms of samples RTE2 and RMS1 are shown to illustrate the typical electrochromic performance of the two groups of films prepared by the two techniques. For both samples, the coloration efficiency, defined as the change in optical density per unit of inserted/extracted charge, reaches a level as high as 0.1 cm² mC⁻¹, which is comparable to the data reported by other groups.[14] Furthermore, transitions between colored and bleached states are still observable after ten thousand cycles. The major difference between the two films is that the J-V loops of RTE2 shrink more remarkably after the same number of switching, even though the driving alternating current (ac) voltage for RTE2 has a lower amplitude of 1.2 V. This implies that the structure of RTE films is relatively unstable. Indeed, as discussed in the following section, the results of structural analyses reveal that the RTE films are more porous.
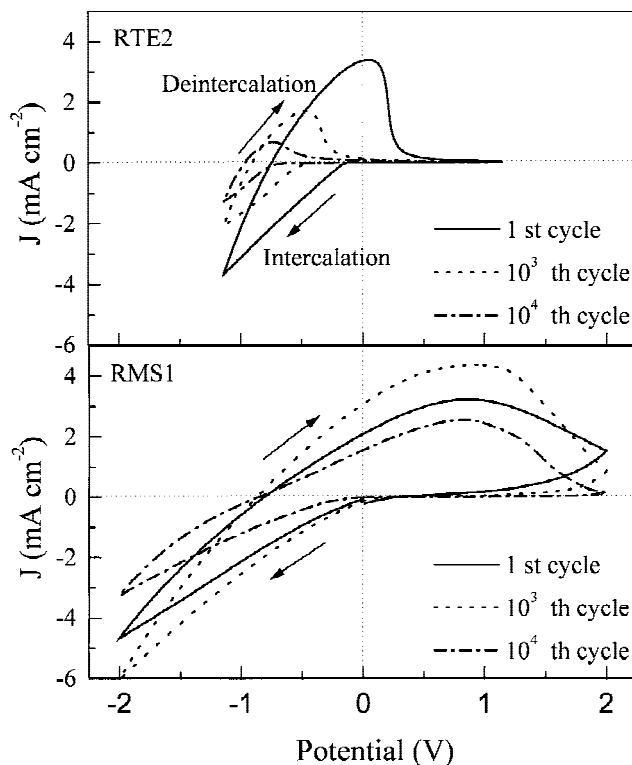


FIG. 1. Cyclic voltammograms of samples RTE2 and RMS1.

### B. Structure

First, let us consider RTE1 deposited by thermal evaporation at the highest $P_{O_2}$ of 10 mtorr and 25 °C. The film has a high O/W ratio of 3.5 (Table I) exceeding that of stoichiometric $WO_3$ phase and is found to be transparent. The XRD spectrum does not show any sharp peaks corresponding to those of crystalline $WO_3$ structure (Fig. 2), but a broad halo covering a 2θ range of about 15° to 35° is found, verifying that the film is amorphous. The small sharp peak at 30.2° is due to the ITO layer of the substrate. The IR absorption spectrum is presented in Fig. 3 in two different scales for wavenumber ranges of 400–1200 cm⁻¹ and 1200–4000 cm⁻¹, respectively. A Band I (labeled Band I) consisting of three components with dip positions at 650, 800, and 900 cm⁻¹ is observed. The first component is close to the IR peak (at 600 cm⁻¹) reported for magnetron sputtered tungsten oxide film, which is assigned to the vibration mode of the disordered W–O framework.[15,16] The second component is close to the two IR bands of crystalline $WO_3$ (at 800 or 807 cm⁻¹).[17,18] The appearance of these two components indicates that the amorphous network in RTE1 has a short range order analogous to that in crystalline $WO_3$. The third component is associated with the stretching vibration of W = O terminal bonds, reported to be present at the surface of atomic clusters.[18] The second band (Band II) is observed to contain two components at 1430 and 1630 cm⁻¹, and the third band (Band III) appears to
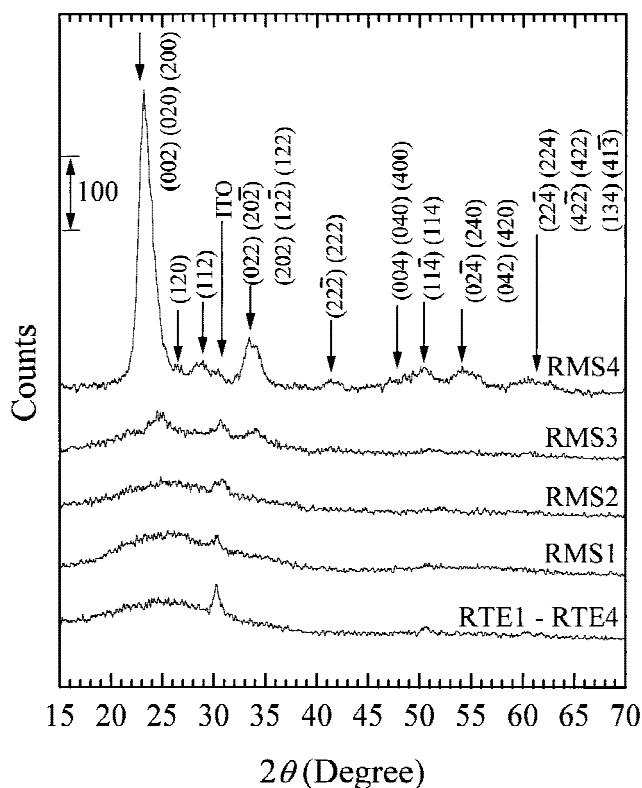
FIG. 2. X-ray diffraction spectra of tungsten oxide films: RTE1 $P_{O_2}$ = 10 mtorr, 25 °C; RMS1 $[O_2]/[Ar]$ = 2, 25 °C; RMS2 $[O_2]/[Ar]$ = 2, $T_s$ = 110 °C; RMS3 $[O_2]/[Ar]$ = 2, $T_s$ = 300 °C; RMS4 $[O_2]/[Ar]$ = 2, $T_s$ = 500 °C.



FIG. 3. Infrared absorption spectra of RTE1, RTE4, RMS1, RMS2, and RMS4.

contain four components at 2800, 3000, 3200, and 3400 cm$^{-1}$. These two bands are associated with the H–O–H deformation and H–O stretching vibration respectively, and are not observed in bulk $WO_3$ crystal. The H–O–H groups come from the surface sorbed water molecules, which continue to dissociate and react with tungsten oxide, resulting in the generation of the H–O groups.[19] The appearance of these two bands indicates that the structure of RTE1 is rather porous so that moisture from air is readily absorbed. This explains the low density of $4.1 \pm 0.32$ g cm$^{-3}$ (Table I) as compared to that of $WO_3$ crystal (7.16 g cm$^{-3}$), which corresponds to a porosity of 43%. The phase contrast AFM image of RTE1, shown in Fig. 4(a), further illustrates that the film has a rough surface and contains pores. The average roughness in the imaged area is 14 nm. The highly porous structure results from the thermal evaporation process where atomic clusters, such as WO, $WO_2$, $WO_3$, $W_2O_6$, and $W_3O_9$, emerge from the melt.[20] These low-energy atomic clusters become immobile after arriving at the unheated substrate and eventually stack loosely to form a porous structure.

Next, we consider the effects of changing $P_{O_2}$ on the RTE samples. RTE1–RTE4 were thermally evaporated at progressively decreasing ambient pressure from
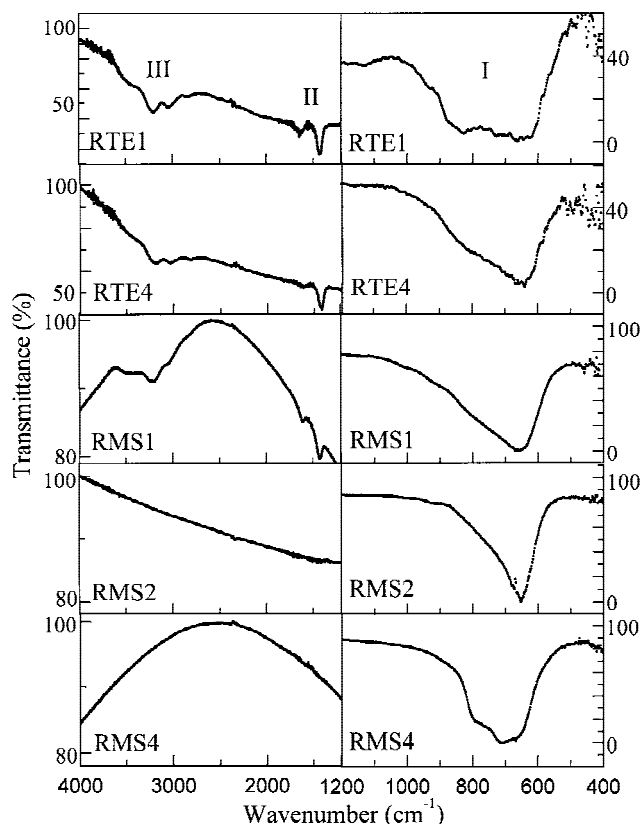
$P_{O_2}$ = 10 mtorr to the background pressure of $2 \times 10^{-3}$ mtorr and at room temperature. All these films have a roughly constant O/W ratio (Table I), and are in an amorphous state (Fig. 2). All their IR spectra contain Band I, II, and III, indicating the presence of $WO_3$-like short range order and pores. However, a decrease in $P_{O_2}$ leads to a weakening of Band II and III (compare the IR spectra of RTE1 and RTE4 in Fig. 3). This is accompanied by a rise in density (Table I), equivalent to a fall in porosity from 41% to 3.7%. In addition, from the phase contrast AFM images of RTE1–RTE4 [Figs. 4(a)–(d)], the average roughness drops from 14 to 2 nm, indicating that the films become smoother and less porous with decreasing $P_{O_2}$.

For the RMS films, let us concentrate on RMS1 first, which was deposited at $[O_2]/[Ar]$ = 2 and room temperature. RMS1 is amorphous (Fig. 2) with an O/W ratio of 3, and is transparent in appearance. The presence of Band I, II, and III in the IR spectrum (Fig. 3) reflects the existence of $WO_3$-like short range order and water absorbing pores in the atomic network. The following evidence indicates that there is a smaller number of pores. First, Band II and III are weaker than those of the RTE films. Secondly, the density reaches $7.7 \pm 0.32$ g cm$^{-3}$, higher than those of the RTE films and close to that of

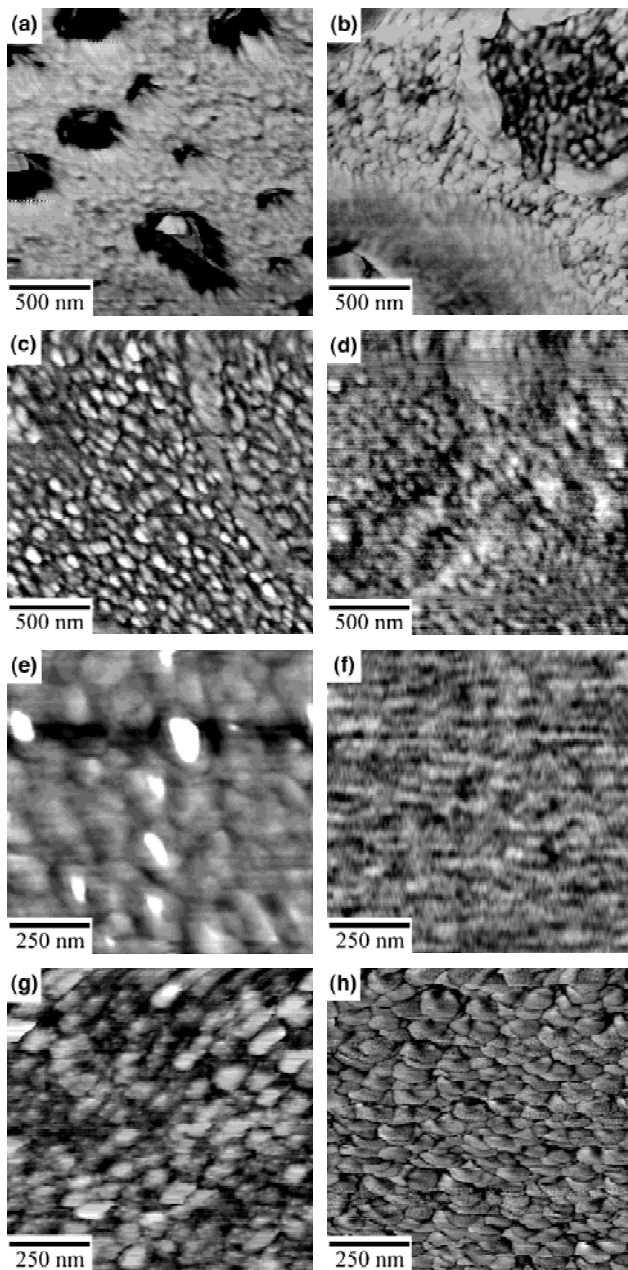1544

J. Mater. Res., Vol. 16, No. 6, Jun 2001

FIG. 4. Phase contrast AFM images recorded from a series of (a–d) reactive thermally evaporated films RTE1–RTE4 and (e–h) a series of reactive magnetron sputtered films RMS1–RMS4.

crystalline $WO_3$, and finally, the AFM image [Fig. 4(e)] shows that RMS1 is rather smooth with a roughness as low as 0.7 nm. RMS1 is smoother than RTE4 because magnetron sputtering involves the condensation of species in atomic scale, which can then be closely packed. Nevertheless, the pores have a significant influence on the mechanical properties, which will be discussed in detail in Sec. IV.C.

We then consider the effects of changing substrate temperature $T_s$ on the RMS samples, RMS2–4 were deposited at progressively increasing $T_s$ from 110 to

500 °C. As shown in Table I, the change in $T_s$ does not alter the O/W ratio and density within the range of experimental error. However, the rise in $T_s$ induces the following two main effects. First, for $T_s \geqslant 110$ °C, Band II and III in the IR spectra associated with water absorbing pores disappear, indicating that the deposits formed at elevated temperature experience equivalently an annealing effect and therefore become much denser. Second, for $T_s \geqslant 300$ °C, the XRD spectra show characteristic peaks of crystalline $WO_3$ structure and the intensity becomes stronger with increasing $T_s$ (Fig. 2), indicating that the films have been crystallized and the grain size becomes larger.[21] The following facts follow. First, Band I in the IR spectra becomes sharper. In particular, two components are identified to be contained in Band I of RMS4, which are attributable to those of crystalline $WO_3$ at 719 and 807 $cm^{-1}$, respectively.[18] Second, the film surface becomes rougher. The average roughness increases from a minimum value of 0.25 nm for RMS2 [just before crystallization occurs, Fig. 4(f)] to 2.78 nm for RMS4 [Fig. 4(h)]. The particle size observed in the AFM micrograph becomes larger ($\approx$70 nm for RMS4) and the boundaries between the particles are much clearer.

Finally, RMS5 and RMS6 deposited at lower $[O_2]/[Ar] = 1.75$ and 1.36 and 25 °C are tungsten rich, such
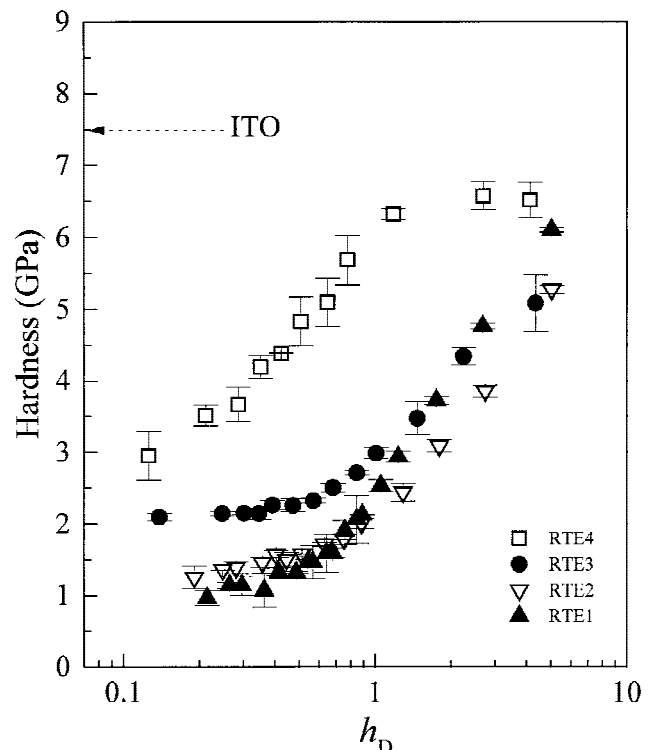


FIG. 5. Normalized penetration depth dependence of the hardness of the RTE films.
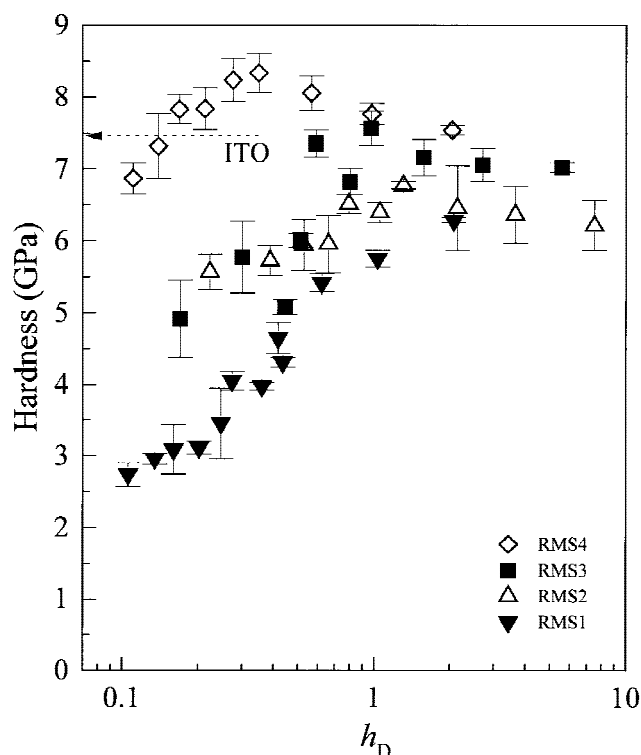
FIG. 6. Normalized penetration depth dependence of the hardness of the RMS films.

that the film density measured is higher due to the heavy atomic weight of tungsten. Furthermore, RMS6 becomes dark brown in color.

## C. Nanoindentation

The nanoindentation hardness of the RTE and RMS films are plotted in Figs. 5 and 6, respectively, as a function of normalized penetration depth $h_D$. The $h_D$ is defined as the contact depth between the tip and the surface divided by the film thickness. This presentation is preferred for comparing data of samples with different thicknesses, since results obtained at small $h_D$ reflect mainly reflect the mechanical properties of the film samples, but contain less contribution from the substrate deformation.

The hardness of RTE1 deposited at the highest $P_{O_2}$ is found to rise markedly with increasing $h_D$ (Fig. 5). The average hardness and elastic modulus obtained at $h_D$ in the range of 0.2–0.3 are the lowest (0.96 and 43.5 GPa) among those of all the samples (Table I). One explanation for the strong contact depth dependence of hardness is that when the tip touches the surface of RTE1, which is very rough (roughness = 14 nm), the contact is first a multi-asperity contact. The theoretical contact area deduced from Eqs. (1) to (3) is larger than the real contact area, such that the measured hardness at shallow contact depth obtained from Eq. (4) is

underestimated.[22] However, this is not the main cause for the rise of hardness in the range of $h_D$ under observation, since the contact depths used are mostly ⩾20 nm (equivalent to $h_D$ ⩾ 0.1 for a film thickness of 177 nm) at which the contact has already become a single-point contact. Another explanation is required. The phase contrast AFM image of RTE1 [Fig. 4(a)] shows extensive porosity. When the indenter tip is driven into the film, the pores collapse and the film is densified progressively at the point of contact.[23] A rise in hardness with increasing $h_D$ thus results. The AFM image confirms this high level of porosity, which can be related to the low hardness.

RTE2 deposited at a lower $P_{O_2}$ shows a complex microstructure [Fig. 4(b)]; it is made of various regions with different gain sizes and porosity. This specimen has a higher average hardness 1.3 GPa at $h_D$ in the range of 0.2–0.3 compared to RTE1, which can be related to a microstructure [Fig. 4(b)] denser than the microstructure of RTE1. The AFM image of RTE3 deposited at a more lower $P_{O_2}$ [Fig. 4(c)] illustrates a uniform distribution of particles; the microstructure is more homogeneous, which correlates with a milder contact depth dependence of hardness, and higher average hardness and elastic modulus at $h_D$ ≈ 0.2 to 0.3 of 2.1 and 54.7 GPa. The image in Fig. 4(d), represents the sample RTE4, deposited at the ultimate background pressure of $2 \times 10^{-3}$ mtorr. The particle sizes are more uniform and the microstructure is denser (lower pore density). It appears that the contact depth dependence of hardness is further weakened, and the high average hardness and elastic modulus (3.2 and 80.1 GPa) at $h_D$ ≈ 0.2 to 0.3 are related to the density of the film, which is the highest among the four RTE films discussed above.

We pointed out that the hardness data of all the four RTE films are constantly lower than that of a blank ITO coated glass substrate (7.5 GPa), even when the indentation depth reaches the film/substrate interface. To explain this feature, one regards the sample as a soft film on hard substrate composite. The nanoindenter starts to measure indentation depth from the contact point, while the penetration depth into the substrate is just roughly equal to the total depth minus the film thickness. To reach a certain total depth, a lower load is required for the soft film on hard substrate composite than that required for a bare hard substrate, such that the measured hardness of the former is constantly lower than that of the latter.

For the magnetron sputtered sample RMS1 deposited at room temperature, the $h_D$ dependence of the hardness of RMS1 is similar to that of RTE4 (Fig. 6), and the average hardness and elastic modulus at $h_D$ ≈ 0.2 to 0.3 do not differ too much from those of RTE4 (Table I). According to the IR data, RMS1 still shows absorption bands associated with pores which absorb water. The

AFM image [Fig. 4(e)] shows that its microstructure is composed of larger particles that appear less compact. The surface is uneven and there are significant particle boundary gaps. For such a structure, intrusion of indenter tip can also cause significant densification with increasing penetration depth, resulting in the prominent depth-dependent hardness and low hardness values as observed.

RMS2 deposited at a higher $T_s$ of 110 °C shows a uniform surface, and particle size distribution is also uniform [Fig. 4(f)]. It is a highly fine-grained material with minimum amount of porosity. Correspondingly, the two IR absorption bands related to absorption of water disappear. Densification of films during indentation as discussed for the above cases is much less significant, so the $h_D$ dependence of hardness is further weakened. The lack of porosity, improvement of compactness of the particles, and uniformity of the particle size are responsible for the prominent rise of the average hardness and elastic modulus ($h_D \approx 0.2$ to 0.3) to the levels of 5.6 and 95.8 GPa, respectively (Table I). Distinctively, the plot of hardness against $h_D$ shows a peak at $h_D$ slightly above 1 (just across the film/substrate interface). This feature appears from pileup of the film surrounding the indenter tip, which is usually observed for indentation of soft film on hard substrate systems. Pileup is induced by the constraint of lateral plastic deformation of a soft film imposed by the relatively undeformable substrate.[24] Equation (4) does not take into account the additional contact area associated with the pileup, such that the theoretical contact area deduced is underestimated. This leads to an apparently higher hardness value, causing the peak in the hardness plot to appear.

RMS3 and RMS4 deposited at higher $T_s$ are crystallized. Their AFM images [Figs. 4(g) and (h)] show that larger grains are formed with sharper boundaries when $T_s$ rises. The following consequences result. First, the average hardness at $h_D \approx 0.2$ to 0.3 rises to 7.8 GPa. Second, the $h_D$ dependence is further diminished because of the lack of pores. Third, a peak in the hardness plot against $h_D$ is observed, but the peak position shifts towards shallower contact depth. This is possibly because the grains start to impose additional constraints on the lateral movement of the film material at relatively shallower depths. Finally, the hardness of RMS4 at deep indentations approaches that of a blank ITO-coated glass substrate (7.5 GPa) since the sample is no longer a soft film on hard substrate system.

RMS5 and RMS6 deposited at decreasing [O₂]/[Ar] = 1.75 and 1.36 (at 25 °C) contain more tungsten and are harder than RMS1 fabricated at the same temperature (Table I). In particular, for the most tungsten-rich sample, RMS6, the hardness and elastic modulus are rather close to those of metallic tungsten, namely, 6 GPa and 410 GPa respectively.[13]

## V. CONCLUSIONS

In conclusion, tungsten oxide films were deposited by reactive thermal evaporation with oxygen ambient pressure as the fabrication parameter, and reactive magnetron sputtering with substrate temperature as the parameter. The film structure ranged broadly from being porous, amorphous to polycrystalline. Electrochromic properties of some film samples from the two groups were demonstrated. The change in the mechanical properties were interpreted by correlating with the structural change observed.

RTE samples are highly porous and amorphous. Decrease in oxygen ambient pressure from 10 mtorr down to the ultimate background pressure of $2 \times 10^{-3}$ mtorr leads to the following results. First, the film structure becomes less porous, such that the density rises and the film surface is smoother. Second, because of the highly porous structure, the intrusion of the indenter tip during this hardness test induces closing of pores at the contact point, such that the hardness of all the RTE films rises considerably with increasing indentation depth. Furthermore, the average hardness and elastic modulus, measured in the $h_D$ range of 0.2 to 0.3, for example, rise correspondingly from low values of 0.96 and 43.5 GPa to 3.2 and 80.1 GPa.

The RMS film deposited at room temperature is amorphous and denser than all of the RTE films. Strong indentation depth dependence of hardness is still observed because a small number of defects are present as confirmed by the emergence of the water-related IR absorption bands, which cause continuous closing of pores and densification of the film material at the contact point. The average hardness and elastic modulus, in the $h_D$ range of 0.2 to 0.3, for example, remain low and are comparable with those of the hardest RTE film. The rise in $T_s$ first causes a decrease in the pore density (e.g., up to 110 °C), and then crystallizes the film structure (e.g., at about 300 °C), and then further enhances the growth of grain size. Along with these structural changes, the hardness becomes less dependent on the penetration depth. Pileup of the film material occurs at the contact point of indentation, giving rise to the appearance of a peak in the plot of hardness against penetration depth. Pileup occurs if the film is not too porous and at the same time is much softer than the substrate. The lateral movement of the film material at the contact point is constrained by the hard substrate. When $T_s$ increases, pileup, and thus the peak in the plot of hardness versus $h_D$, occurs at shallower indentation depth because the formation and growth of grain size could impose additional constrains to the lateral movement of the film material. Furthermore, when the average hardness within the same range of $h_D$ (e.g., 0.2 to 0.3) is compared, a film deposited at higher $T_s$ is harder.

## ACKNOWLEDGMENTS

## REFERENCES

1. K. von Rottkay, M. Rubin, and S-J. Wen, Thin Solid Films **306,** 10 (1997).
2. P.M.S. Monk, R.J. Mortimer, and D.R. Rosseinsky, Electrochromism: Fundamentals and Applications (VCH Publishers, New York, 1995), p. 15.
3. C. Bechinger, J.N. Bullock, J-G. Zhang, C.E. Tracy, D.K. Benson, S.K. Deb, and H.M. Branz, J. Appl. Phys. **80,** 1226 (1996).
4. Q. Zhong, J.R. Dahn, and K. Colbow, J. Electrochem. Soc. **139,** 2406 (1992).
5. C.G. Granqvist, Solid State Ionics **53–56,** 479 (1992).
6. K. Kaneda and S. Suzuki, Jpn. J. Appl. Phys. **30,** 1841 (1991).
7. L.H.M. Krings and W. Talen, Sol. Energ. Mater. Sol. C **54,** 27 (1998).
8. M. Denesuk, J.P. Cronin, S.R. Kennedy, and D.R. Uhlmann, J. Electrochem. Soc. **144,** 888 (1997).
9. L. Su, J. Fang, Z. Xiao, and Z. Lu, Thin Solid Films **306,** 133 (1997).
10. C.G. Granqvist, Handbook of Inorganic Electrochromic Materials (Elsevier, Amsterdam, The Netherlands, 1995), p. 33.
11. D.A. Shirley, Phys. Rev. B **5,** 4709 (1972).
12. G.K.H. Pang, K.Z. Baba-Kishi, and A. Patel, Ultracroscopy **81,** 35 (2000).
13. W.C. Oliver and G.M. Pharr, J. Mater. Res. **7,** 1564 (1992).
14. S.F. Cogan, T.D. Plante, E.J. Anderson, and R.D. Rauth, Proc. SPIE **562,** 23 (1985).
15. A. Azens, C.G. Granqvist, E. Pentjuss, J. Gabrusenoks, and J. Barczynska, J. Appl. Phys. **78,** 1968 (1995).
16. N. Yoshiike, and S. Kondon, J. Electrochem. Soc. **130,** 2283 (1983).
17. C.G. Granqvist, Handbook of Inorganic Electrochromic Materials (Elsevier, Amsterdam, The Netherlands, 1995), p. 41.
18. Y. Shigesato, A. Murayama, T. Kamimori, and K. Matsuhiro, Appl. Surf. Sci. **33/34,** 804 (1988).
19. C.G. Granqvist, Handbook of Inorganic Electrochromic Materials (Elsevier, Amsterdam, The Netherlands, 1995), p. 43.
20. N.P. Vas'ko, Yu.G. Ptushinskii, and B.A. Chuikov, Surf. Sci. **14,** 448 (1969).
21. Q. Zhong, J.R. Dahn, and K. Colbow, Phys. Rev. B **46,** 2554 (1992).
22. M.S. Bobji and S.K. Biswas, J. Mater. Res. **14,** 2259 (1999).
23. T.Y. Tsai, J. Vlassak, and W.D. Nix, J. Mater. Res. **14,** 2196 (1999).
24. T.Y. Tsai, W.C. Oliver, and G.M. Pharr, in *Thin Films: Stress and Mechanical Properties VI,* edited by W.W. Gerberich, H. Gao, J-E. Sundgren, and S.P. Baker (Mater. Res. Soc. Symp. Proc., **436,** Pittsburgh, PA, 1997), pp. 207–212.